

pubs.acs.org/ac Article

Shear Stress-Induced Microstructure Remodeling of Human Bicuspid Aortopathy Revealed by Nonlinear Optical Microscopy

Lili Zhang,[#] Yuntao Lu,[#] Wencong Hong,[#] Shuo Cong, Jiaying Li, Huan Liu, Chunsheng Wang, Lai Wei, Jianpeng Ao,* Wenshuo Wang,* and Minbiao Ji*



Cite This: https://doi.org/10.1021/acs.analchem.5c04657



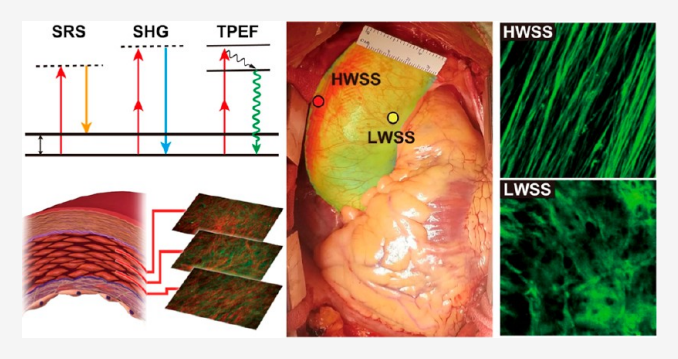
ACCESS I

III Metrics & More

Article Recommendations

s Supporting Information

ABSTRACT: Congenital defects and abnormal hemodynamics are widely accepted theories in bicuspid aortic valve (BAV)-associated aortopathy. However, current clinical criteria for surgical intervention in BAV patients fall short of direct correlation with neither factor. Here, we applied nonlinear optical (NLO) microscopy to investigate the microstructural changes of the aortic wall associated with bicuspid aortopathy at different stages. Fresh aortic specimens were collected from 24 study patients and assessed by NLO scanning layer-by-layer to probe the distribution of the extracellular matrix and smooth muscle cells (SMCs). NLO images demonstrated near-perfect concordance with traditional histology (Masson's and Weigert's staining), affirming its reliability for



histologic assessment. In BAV-associated aortic dilatation (BAV-AD), collagen fibers exhibited better alignment with a helix-like pattern compared to tricuspid aortic valve (TAV) patients, while their content was markedly reduced relative to nondilated BAV (BAV-NA) cases. Notably, both collagen and elastin fibers in BAV patients displayed more ordered alignment in regions subjected to high wall shear stress than in low wall shear stress regions. Quantitative analysis of fiber anisotropy and relative abundance revealed distinct interpatient and spatial variations in collagen organization, underscoring the complex biomechanical landscape associated with aortic remodeling. Our results demonstrate that rapid and precise tomography of aortic architecture could be realized by NLO microscopy, serving as a potential histological marker to guide surgical intervention in bicuspid aortopathy.

■ INTRODUCTION

Bicuspid aortic valve (BAV) is the most common congenital heart defect worldwide, occurring in 1-2% of the general population. It is associated with a series of aortopathy, among which dilatation of the ascending aorta is commonly manifested,² but the underlying mechanism is not defined. In all BAV patients, the incidence of catastrophic aortic outcomes such as dissection and rupture has been estimated to be much higher than in the general population, bringing precise determination of optimal surgical intervention timing of aorta, defined as the time point when the risk of conservative management exceeds the risk of surgery, to a vital position. The aortic wall is composed of the intima, adventitia, and media with multiple layers. Although classical histology with Masson's and Weigert's stains is capable of identifying the main components in aorta, such as collagen fibers, elastic fibers, and smooth muscle cells (SMCs), it is time-consuming and inapplicable in the intraoperative settings. Hence, it is difficult and controversial, especially when the patient is indicated to have aortic valve replacement due to the severe valvular problem. 4 Currently, cardiovascular surgeons primarily rely on the measured aortic diameter or their clinical experience. 5,6 However, the cutoff value, 4.5 cm of the

ascending aorta's diameter, neither has convincing evidence nor adequately reveals the underlying pathology of aortopathy. Therefore, imaging tools that provide accurate and rapid intraoperative histopathological profiles of healthy and damaged aortic tissues are of critical importance.

Label-free nonlinear optical (NLO) microscopy techniques, including two-photon excited fluorescence (TPEF), second harmonic generation (SHG), and stimulated Raman scattering (SRS) microscopy (Figure 1), have become powerful tools for diverse biomedical research studies.^{7–10} These microscopy techniques rely on distinct nonlinear optical processes arising from light-mattering interactions, each offering unique molecular specificity within biological samples.^{9,11–13} TPEF is sensitive to endogenous fluorophores, including NAD, FAD, elastin fibers, etc.^{8,14,15} In aortic tissues, elastin fiber is the main source of TPEF. SHG is a coherent second-order nonlinear

Received: July 30, 2025 Revised: October 23, 2025 Accepted: October 23, 2025



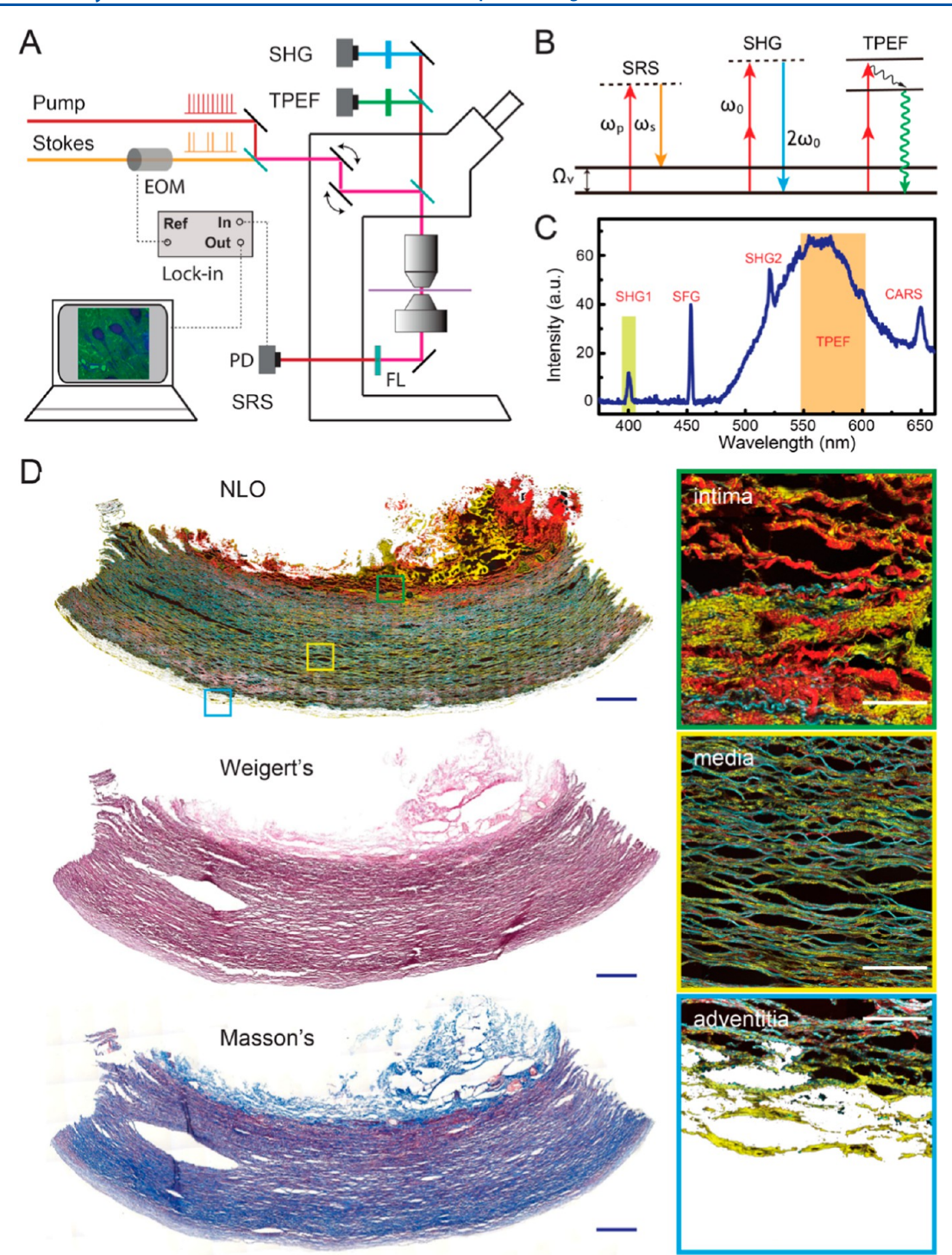


Figure 1. (A) Optical layout of the multimodal NLO microscopy. (B) Energy diagram and optical transitions of SRS, SHG, and TPEF. (C) A typical spectrum of aortic tissue showing various nonlinear optical signals. (D) The same cross-section plane of ascending thoracic aorta displayed in Masson's and Weigert's stains. Zoomed-in NLO images demonstrate detailed architecture at different locations of the aorta cross-section, such as collagen fibers (red), elastin fibers (cyan), and SMCs (yellow). Scale bars: 1 mm (D, left), 200 μ m (D, right). EOM: electro-optical modulator; FL: filter; Lock-in: lock-in amplifier; PD: photodiode.

optical process, which requires the breaking of inversion symmetry and exhibits high sensitivity to type I collagen fibers in biological tissues. SRS microscopy is a more recently developed coherent Raman technique that boosts Raman signal through stimulated emission, enabling rapid imaging of cells and tissues with high molecular specificity and spatial resolution. In aortic specimens, SRS primarily maps the distribution of smooth muscles, which are rich in C–H

bonds.²⁴ All of these label-free NLO techniques have the potential to be adapted in intraoperative settings and may provide rapid diagnosis on fresh, unprocessed tissues, both ex vivo and in vivo. In addition, the intrinsic optical sectioning capability allows layer-by-layer tangential-plane scanning of aortic tissue histoarchitectures, thereby generating comprehensive three-dimensional information on the aortic wall. Despite previous efforts on applying these imaging techniques

for label-free tissue histology of many types of human diseases, 25-28 the potential for integrating their advantages to help evaluate vascular damage has never been rigorously investigated.

In this study, we have applied a multimodal NLO microscopy with integrated TPEF, SHG, and SRS to generate multichromatic images of aortic media, capturing the spatial distributions and structural characteristics of smooth muscle cells, elastin fibers, and collagen fibers. We aimed to demonstrate that the ascending aorta of trileaflet aortic valve (TAV) donors and BAV patients develop distinct histological features in response to regional hemodynamic differences, which could be early signs of ascending aorta pathologies in patients with BAV-associated aortopathy.

METHODS

Tissue Collection. All tissue samples from total 24 patients were harvested at Zhongshan Hospital, Fudan University, Shanghai, between April 2018 and August 2020 including 6 normal TAV patients, 9 BAV-associated aortic dilatation (BAV-AD) patients, and 9 nondilated BAV (BAV-NA) patients. The Ethics Committee of Zhongshan Hospital approved the study (B2018-285R) in 2018. All patients or their legal representatives were fully informed and given written consent before the study. The investigation conformed with the principles outlined in the Declaration of Helsinki. Ascending aortic specimens of normal TAV patients as well as BAV-NA patients were collected from heart transplant donors without aortic disease and with TAV or BAV, respectively. Meanwhile, specimens of BAV-AD patients were collected during elective Wheat's or Bentall's surgery from patients with BAV-associated severe aortic stenosis or aortic regurgitation and accompanied by ascending thoracic aortic dilatation (diameter >45 mm).

Sample Preparation. For thin tissue sections, frozen tissues were sectioned using a fast cryotome (CM1950, Leica) into a series of adjacent 4 μ m, 10 μ m, and 4 μ m thick slices. The middle 10 μ m slice was used for NLO imaging directly without additional processing, and the 4 μ m slices on both sides were sent for Masson's and Weigert's staining, respectively. To perform both SRS imaging and Weigert's staining on the same frozen tissue section, the 4 μ m slice was first imaged with NLO microscopy, followed by Weigert's staining. These tissue sections were used to correlate NLO imaging with traditional histology staining.

For fresh tissue preparation, upon excision and intima stripping, fresh aortic tissues were sealed between two glass coverslips and a perforated glass slide (0.5 mm thickness) to maintain a constant thickness. Fresh tissues were imaged directly with NLO microscopy. For quantitative analysis, all tissue images were taken at the same depth of 15 μ m.

Histology Staining. Specimens designated for histology were sectioned, fixed in 10% buffered formalin, and embedded with paraffin. Sections were processed by Masson's trichrome or Weigert's elastic stain, using a commercially available kit from Servicebio Inc. and Solarbio Inc. and following the manufacturer's instructions. With Masson's stain, collagen fibers stained blue and SMCs pink. With Weigert's stain, collagen fibers, elastin fibers, and SMCs appear pink, dark blue, and yellow, respectively.

Multimodal Nonlinear Optical Microscopy. SRS, TPEF, and SHG imaging were integrated into the same platform via the multimodal system shown in Figure 1. The

experimental setup was based on a previously described system. ^{25,29-31} Briefly, pulsed femtosecond laser beams from a commercial optical parametric oscillator (OPO) laser (Insight DS+, Newport) served as the light source. For SRS imaging, the fundamental 1040 nm laser was set as the Stokes beam (\sim 150 fs) and the tunable OPO output (690–1300 nm, \sim 120 fs) as the pump beam. The intensity of the 1040 nm beam was modulated at 20 MHz using an electrooptical modulator (EOM). The two laser beams were stretched to picoseconds via SF57 glass rods for spectral resolution and combined through a dichroic mirror (DMSP1000, Thorlabs), spatially and temporally overlapped, delivered into the laser-scanning microscope (FV1200, Olympus) and focused tightly onto the samples. The SRS signal was detected by a back-biased photodiode (PD) and demodulated with a lock-in amplifier (LIA) (HF2LI, Zurich Instruments). The 800 nm beam was the main excitation source for TPEF and SHG, which exhibit significantly different spectra and can be separated using proper optical filters (Figure 1A-C): SHG with a narrow bandpass filter (FF01-405/10, Semrock) and TPEF with a broad bandpass filter (FF01-575/59, Semrock). To minimize the orientational effects of fibers, we applied circular polarization for both pump and Stokes beams without any detection polarizer. 32 All three modalities were imaged simultaneously, with SRS collected in transmission mode and SHG and TPEF in epi mode. The imaging speed used throughout the experiments was 2 μ s per pixel, with each image containing 512×512 pixels, i.e., ~ 1 s/frame. We used a 60× objective (Olympus, UPLSAPO 60XWIR, NA 1.2 water) with a lateral resolution of ~400 nm and an axial resolution of \sim 2 μ m. Laser powers of 20 mW for the pump and 10 mW for Stokes pulses were used to image fresh tissue sections.

Quantification of Fiber Contents. Each image (including SHG, TPEF, or SRS) was imported into ImageJ software (NIH, USA) for quantitative analysis. Pixel intensity histogram was generated by a plugin program. Since the total protein content measured by SRS exhibits much more stable intensity across sample groups, we took SRS intensity as a reference to quantify collagen and elastin fiber contents. The relative quantification of collagen fiber contents was determined by the ratio between the mean intensity of SHG to that of SRS, and the relative quantification of elastin fiber contents was determined by the ratio between the mean intensity of TPEF to that of SRS.

Quantification of Fiber Anisotropy. The two-dimensional fast Fourier transform (2D-FFT) approach was used to measure fiber alignment in NLO images³² (Figure S1). The 2D-FFT function converts spatial information in NLO images into a frequency domain that maps the rate at which pixel intensities change in the spatial domain. The resulting frequency plot contains a cluster of white pixels that are concentrated in a symmetrical circular pattern around the origin. A circular projection is placed on the frequency plot (using the ImageJ circular marquee tool). Using the ImageJ oval profile plug-in, the pixel intensities are then summed along the radius for each angle of the circular projection $(0-360^{\circ})$. The summed pixel intensities for each radius are then plotted against the corresponding angle of acquisition (position of the radial projection on the circular projection) to produce a 2D FFT alignment plot. All NLO images were stored and analyzed as uncompressed .TIF files to preserve the image integrity.

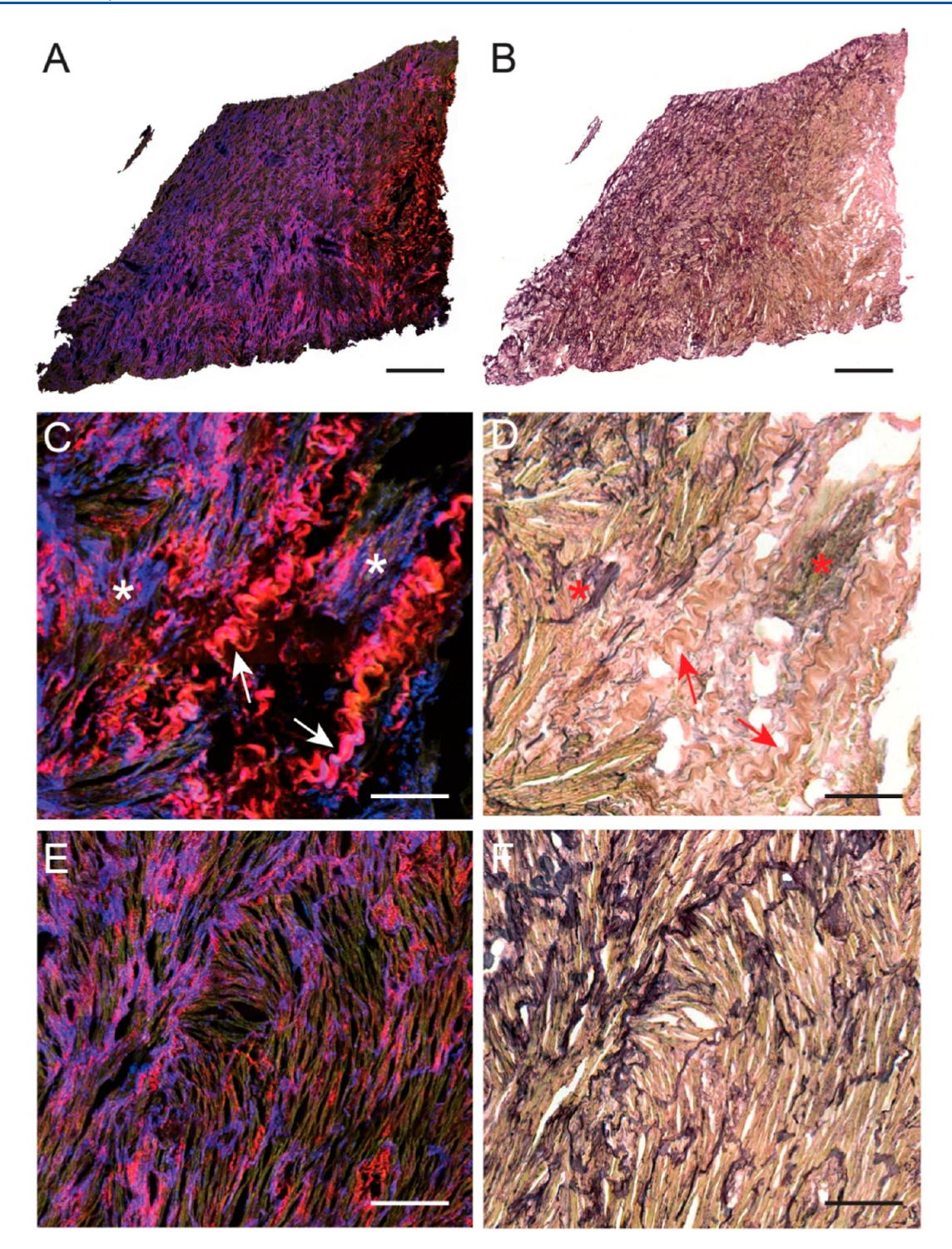


Figure 2. (A,B) En-face aortic tissue imaged with NLO microscopy and Weigert's stain on the same section. (C-F) Zoomed-in images showing detailed morphological and chemical correlations between NLO and Weigert's. In NLO, collagen fiber, elastin fiber, and SMCs are colored red, blue, and yellow, respectively. In Weigert's stain, collagen fiber, elastin fiber, and SMCs are colored pink, blue, and yellow, respectively. Scale bars: 1 mm (A,B), 200 μ m (C-F).

RESULTS AND DISCUSSION

Label-Free Optical Characterization of Human Aortic Tissues. The pathological and biomechanical properties of the aortic wall are determined by its histoarchitectures and chemical compositions, including elastin fibers, collagen fibers, and smooth muscle cells (SMCs), which can be revealed by multimodal NLO microscopy. The optical layout of our integrated multimodal NLO system is illustrated in Figure 1A,

where three types of NLO (SRS/SHG/TPEF) signals can be simultaneously acquired. Their energy diagrams and corresponding optical transitions of the three types of NLO are illustrated in Figure 1B. SRS amplifies the weak Raman signal by 3–5 orders of magnitude via stimulated emission from the Stokes beam, enabling chemical specific imaging based on the vibrational modes of intrinsic biomolecules (such as lipids and protein). In this study, SRS images taken at 2930 cm⁻¹ (CH₃

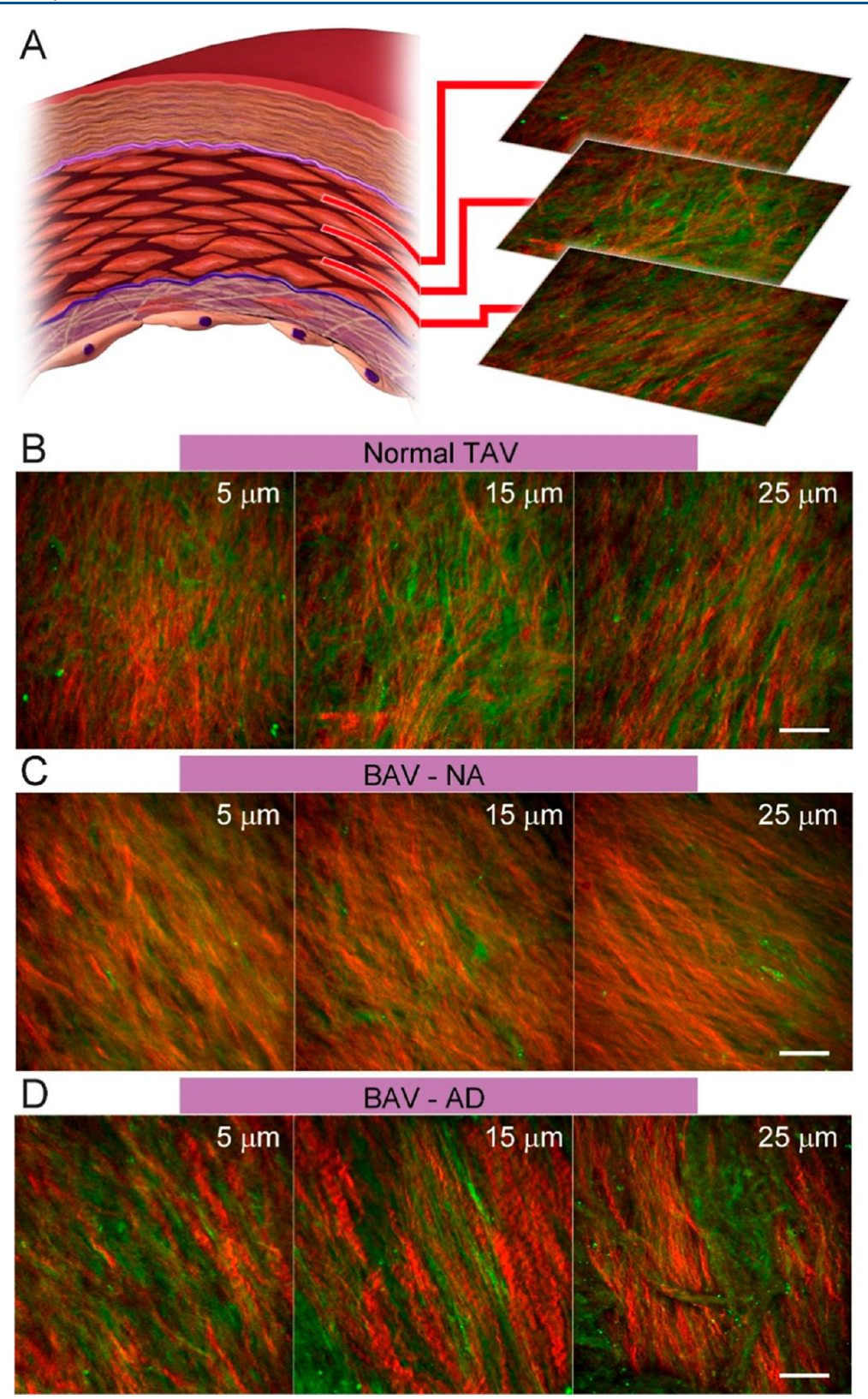


Figure 3. (A) Schematics of the captured image from different depths of the aorta media by NLO microscopy. (B–D) Representative images demonstrating typical collagen (red) and elastin (green) fibers distribution and orientation in the aorta media of normal TAV patient (B), BAV-NA patients (C), and BAV-AD patients (D). Scale bars: $30 \mu m$.

stretching mode) were used to quantify the total protein content of SMCs and extracellular matrix (ECM); SHG images were generated by type I collagen fibers with breaking inversion symmetry; and the TPEF channel imaged the

autofluorescence of elastin fibers in aortic tissues (Figure 1B). A typical multimodal NLO spectrum from aortic tissue is shown in Figure 1C under the excitation of 802 nm (pump) and 1040 nm (Stokes), showing various nonlinear optical

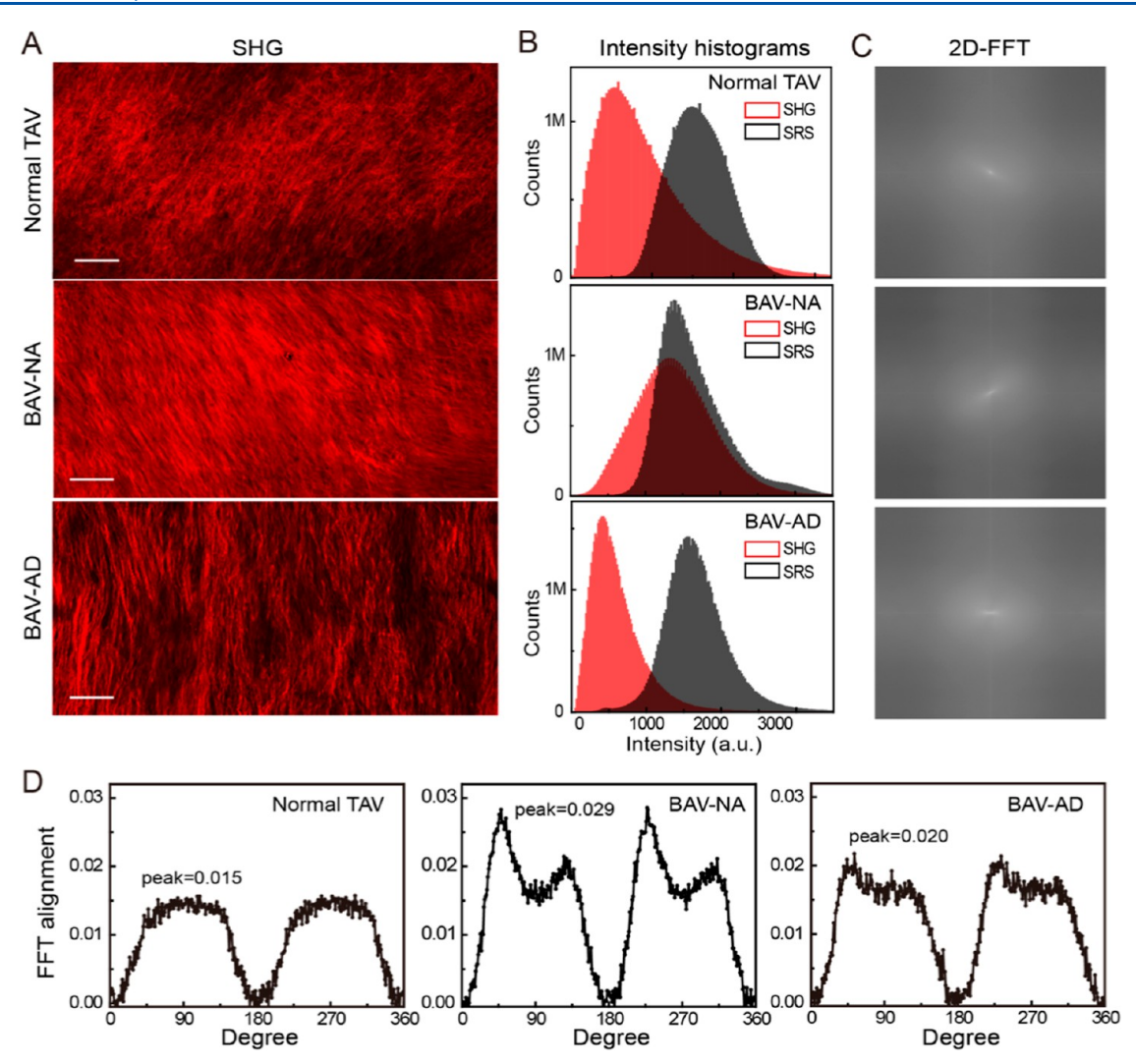


Figure 4. (A) Typical large-scale SHG images of the aorta media from normal TVA, BAV-NA, and BAV-AD patients by NLO microscopy. (B) Intensity histograms of SHG (red) and SRS (black) images of the aorta media from the three groups. (C) 2D-FFT maps converted from the SHG images in (A). (D) 2D-FFT alignment plots of SHG images. Scale bars: 200 μ m.

signals. The sharp peaks at 401 and 520 nm are the SHG signals of the pump and Stokes, respectively. The sharp peaks at 453 and 653 nm are the sum frequency generation (SFG) and coherent anti-Stokes Raman scattering (CARS) signals contributed from both pump and Stokes pulses, whereas the broad spectral feature from 500 to 650 nm is the TPEF signal induced by two-photon absorptions. To avoid crosstalk between different types of NLO signals, only the peak at 401 nm was detected as the SHG channel with a narrow bandpass filter (FF01-405/10, Semrock), the spectral range of 545–605 nm was collected as the TPEF channel with a bandpass filter (FF01-575/59, Semrock), and the SRS channel was detected through demodulation of the pump beam intensity using a lock-in amplifier (Figure 1A and C).

To assess the ability of NLO microscopy to reveal normal histoarchitectures of human aortic tissues, we first imaged the cross-section of a sample obtained from a heart transplant donor with TAV and a normal ascending aorta (Figure 1D). The smooth muscle cell (SMC), collagen, and elastin fibers were imaged by SRS (yellow), SHG (red), and TPEF (cyan), respectively. Then, it was compared to Masson's and Weigert's stained images of adjacent thin frozen sections (Figure 1D, left). It can be seen that not only the overall morphologies of

the tissues imaged by the three methods agree well with each other but also the distributions of the chemical components match well. For instance, all methods found that the collagen fibers usually form more in both adventitia and intima of the aortic wall, and the elastin fibers tend to appear more in the media of the aorta. Magnified NLO images at different locations clearly show detailed morphologies of collagen and elastin fibers without any exogenous stain (Figure 1D, right).

To further demonstrate that NLO microscopy could provide equivalent histological information as Weigert's stain and could also image the face of aortic walls, we performed both modalities imaging on the same frozen tissue section. NLO imaging was first performed without introducing any disturbance to the specimen, followed by Weigert's staining. Both images at different magnifications are shown in Figure 2. Images of the whole section are compared in Figure 2A and B, showing the perfectly matched morphologies of the two imaging methods. More importantly, it can be seen from NLO images that collagen fibers deposit more heavily on the right side of the tissue (red, SHG), while elastin fibers appear more on the left (blue, TPEF), which agree with the Weigert's stain, showing pinkish on the right and dark blueish on the left.

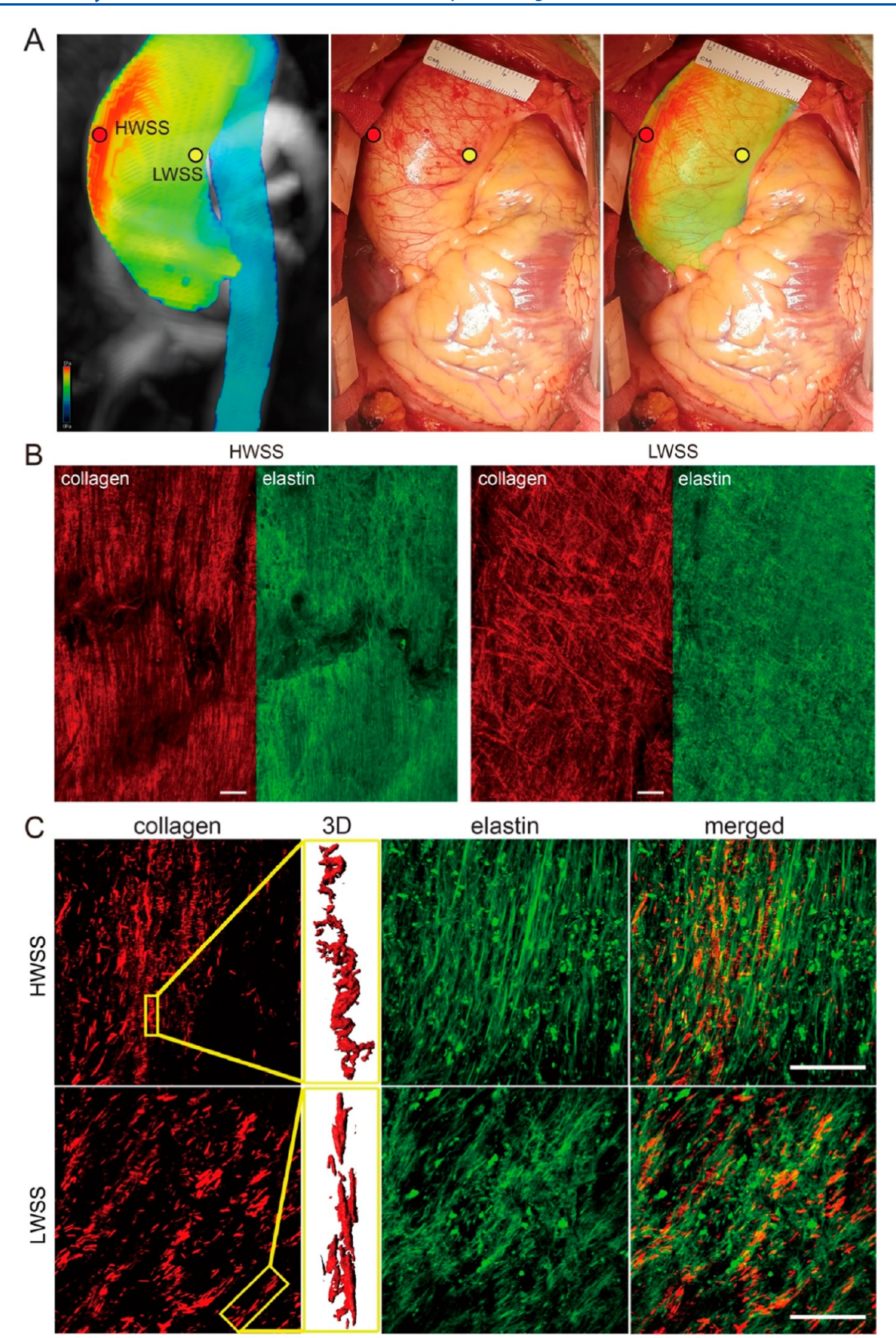


Figure 5. (A) CMR 4D flow pattern in the ascending aorta distal to the aortic valve of BAV-AD patients before operation (left panel), HWSS area (red dot), and LWSS area (yellow dot) were marked in the bright-field image (middle panel) and merged image (right panel). (B) Representative large-scale images of HWSS and LWSS areas marked in (A) using NLO microscopy. (C) The magnified regions of interest, from left to right, are collagen fiber (Red) and its local 3D reconstruction (inside yellow frames), elastin fiber (Green), and merge of collagen and elastin fiber. Scale bars: $100 \ \mu m$ in (B) and $50 \ \mu m$ in (C).

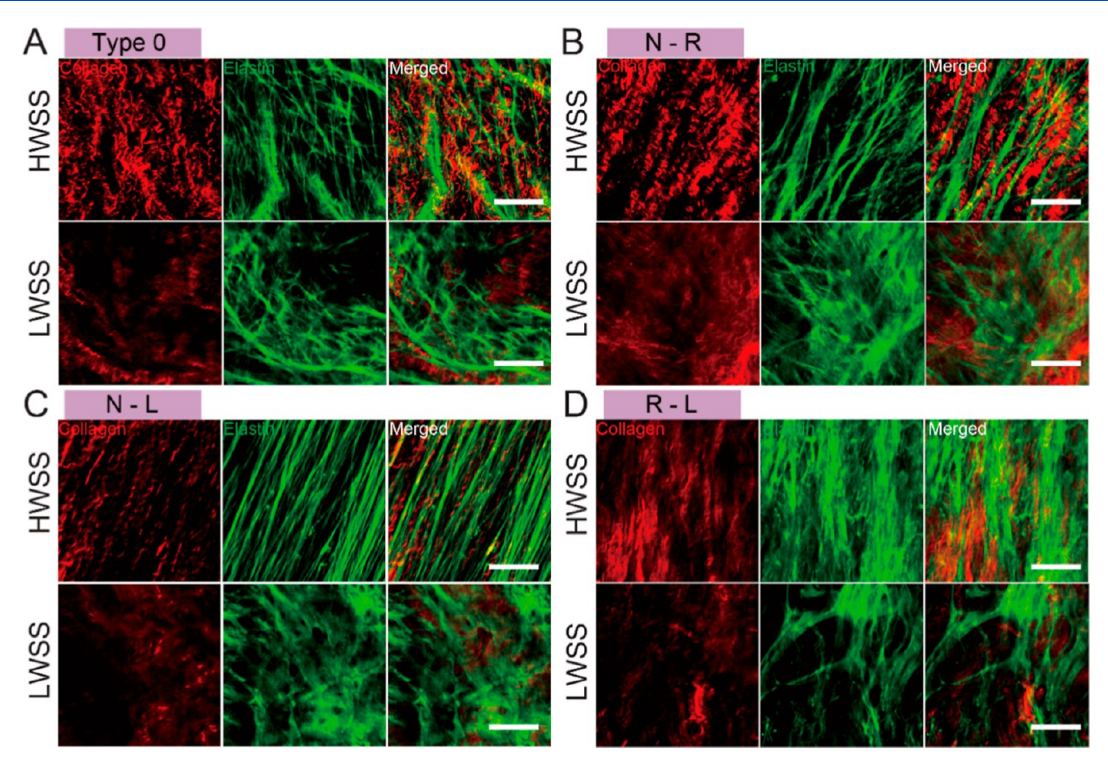


Figure 6. Representative NLO images of HWSS and LWSS area, measured by CMR ascending aortic 4D flow pattern, of different bicuspid aortic valve types. (A) Type 0 (valve with no raphe). Type 1 (valve with one raphe) includes: (B) N-R; (C) N-L; and (D) R-L. N, noncoronary sinus; R(L), right(left) coronary sinus. Scale bars: 50 μ m.

Furthermore, zoomed-in images proved that NLO images and Weigert's staining reveal almost identical structures of collagen fibers (arrows, Figure 2C and D), elastin fibers (asterisks, Figure 2C and D), and SMCs (Figure 2E and F). It is even evident that NLO microscopy is more sensitive in imaging collagen fibers as its pink stain does not provide strong contrast in the Weigert's images (Figure 2C–F). These results on thin tissue sections verified that NLO images could reveal the same critical histological features as standard histopathology in a label-free manner, which provided the basis for studies on fresh tissues.

Revealing Histoarchitectural Changes of Fresh Aortic Tissues in BAV Patients. It is known from the literature that aortopathy in BAV disease often refers to progressive dilatation of the ascending aorta in which medial degeneration plays a vital role. Therefore, to evaluate the ability of NLO microscopy to detect the matrix architecture of the aortic media as well as testify the aforementioned medial remodeling in BAV disease, we then imaged aortic media samples of normal TAV, BAV-NA, and BAV-AD patients at different depths from the intima-face of tunica media (Figure 3A). Representative images of collagen (red) and elastin (green) fibers at depths of 5, 15, and 25 μ m were shown in Figure 3B—D. The contents and arrangements of fibers showed a remarkable difference across samples, while mild variations were found on images at different depths from the same patient.

To further illustrate the differences among patient types, large-scale images at a depth of 15 μ m were demonstrated in Figure 4A. Typically, we found a considerably higher content of collagen fibers in BAV-NA patients' aortic media than in normal TAV patients (Figure 4A), whereas BAV-AD patients seemed to bear a loss of collagen fibers, and interestingly, these collagens displayed a bundle agglomeration and helical

morphology, which could be interpreted as a retraction after tension exceeding breaking threshold. These large-scale SHG images (Figure 4A) and their corresponding SRS images (Figure S2) were imported into ImageJ software (NIH, USA) for quantitative analysis. Pixel intensity histograms were generated by plugin program and shown in Figure 4B. Note that SRS intensity resulting from total protein contents appears relatively stable across different sample groups (Figure S2), and it was used as reference for fiber quantification in the subsequent analysis (Methods). Quantitative histograms agreed with the compensatory hyperplasia of collagen fibers in BAV-NA patients and the loss of collagen fibers in BAV-AD patients (Figure 4B).

To quantify the arrangement of fibers, the 2D FFT function converted the SHG grayscale images into frequency domain plots defined mathematically, which map the rate at which pixel intensities change across the images (Figure 4A and C). The amplitude and phase angle of FFT plots, respectively, carried the intensity and shape information on the images. The frequency plot produced by NIH ImageJ software places lowfrequency pixels at the center, which corresponded to domains within the image that contain pixels of similar intensities. Highfrequency pixels are placed away from the origin and toward the periphery of the frequency plot, which corresponded to spatial domains that exhibit abrupt changes in pixel intensity. Compared to the BAV patients, the frequency plot of a normal TAV patient contained a cluster of more white pixels that are concentrated in a symmetrical, circular pattern around the origin, indicating its relative random fibers (Figure 4C). Summing up pixel intensities against the corresponding phase angle produced 2D FFT alignment plots, and the symmetrical property supported the sufficient analysis for 0° to 180° (Figure 4D). During summation, the preferentially arrayed pixels acted to increase the summed pixel intensity value along

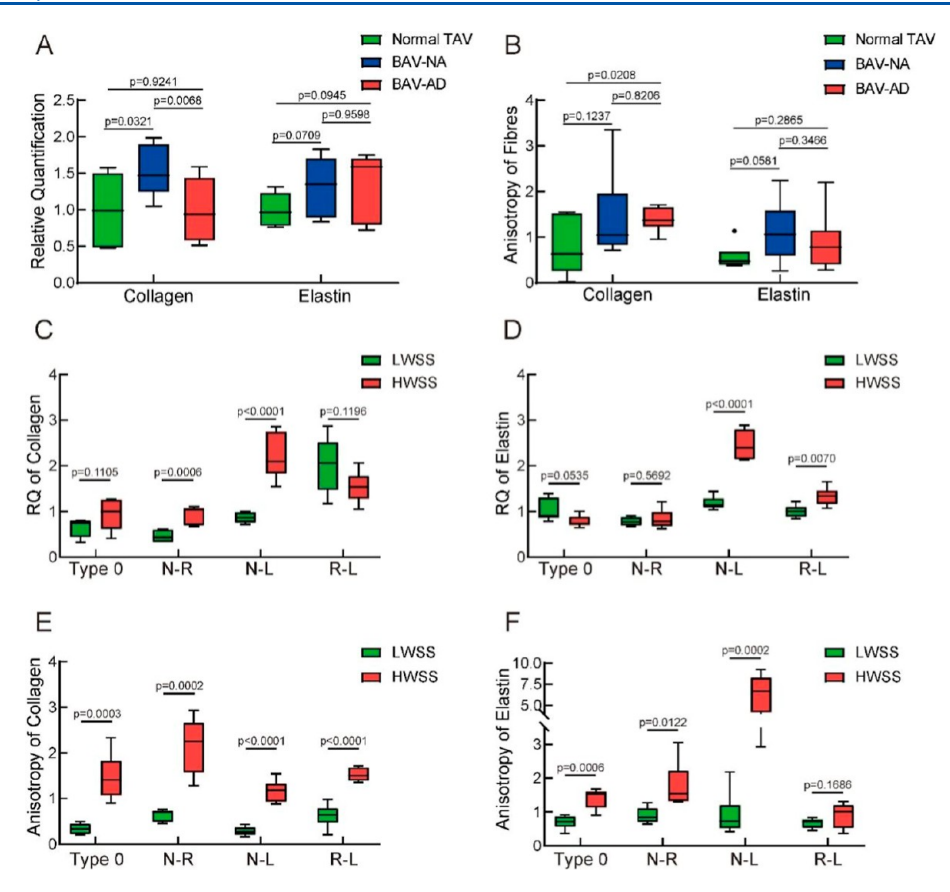


Figure 7. Quantitative analysis. (A) Relative quantification (RQ) of the luminous intensity of collagen and elastin fibers in normal TAV, BAV-NA, and BAV-AD patients. (B) Alignment of collagen and elastin fibers in normal TAV, BAV-NA, and BAV-AD patients. (C,D) Relative quantification value of collagen and elastin fibers in HWSS and LWSS regions of different BAV types, respectively. (E,F) Anisotropy of collagen and elastin fibers in HWSS and LWSS regions of different BAV types, respectively. n = 6 (Normal-TAV), 9 (BAV-NA), 9 (BAV-AD). Bars represent mean \pm SD.

ı

a defined axis, producing a prominent peak in the 2D FFT alignment plot. The degree of alignment presented in fiber images were reflected by the height and overall shape of the most prominent peaks presented in the alignment plots. In contrast to normal TAV patients, the higher and narrower peak in both BAV-NA and BAV-AD patients indicated a highly oriented fiber architecture (Figure 4D). This demonstrates the ability of NLO microscopy to detect specific histopathological changes of BAV aortopathy and also indicates the diagnostic value of collagen fibers.

Stress-Induced Alignments of Fibers in Ascending Aorta. Valve-related hemodynamics, rather than genetic defects, is increasingly accepted as the primary contributor to the progression of aortopathy.³⁴ To rule out the possibility of the genotype effect, we performed NLO imaging on different regions of BAV-AD patients' ascending aortas according to the wall shear stress (WSS), which is considered to correlate with aortic wall remodeling.³⁵ According to the wall shear stress heat map provided by the four-dimensional cardiovascular magnetic resonance (CMR 4D) flow pattern (Figure 5A), we were able to identify the highest wall shear stress (HWSS) and lowest wall shear stress (LWSS) locations and collected the corresponding specimens during operation (Figure 5A). Both HWSS and LWSS specimens from the same patient were imaged by NLO microscopy, and the typical large-scale and magnified SHG and TPEF images were shown in Figure 5B,C. Consistent with our expectations, both collagen and elastin fibers of HWSS regions revealed, to some extent, highly oriented patterns compared to those of LWSS regions (Figure

5B), indicating the possible actions of the hemodynamic factor. In the 3D reconstructed image, we found consistent collagen fiber morphology, including both straight and wavy structures (Figure 5C and Video S1). In LWSS regions, collagen fibers exhibit more random orientation, while HWSS regions show straighter, more oriented fibers, reflecting local remodeling due to elevated hemodynamic stress. This supports the theory of hemodynamics that asymmetrical fiber overstretch is in response to high wall steer stress rather than genetic defects.³⁴

Moreover, the presence of BAV fusion was reported to influence the regional wall shear stress distribution and systolic flow eccentricity. 36 To further evaluate the general applicability of our discovery by NLO microscopy, we also imaged dilated ascending aorta specimens from 4 patients, caused by different major phenotypes of BAV (Figure 6), namely, Type 0, N-R, N-L, and R-L, according to the Sievers classification.³⁷ Type 0 means aortic valve with no raphe; type 1 (valve with one raphe) includes N-R, N-L, and R-L, where N represents noncoronary sinus and R(L) represents right(left) coronary sinus. HWSS and LWSS sites of BAV-AD patients' ascending aorta were measured as the procedure mentioned above. Typical magnified images are shown in Figure 6. A remarkable alignment of collagen and elastin fibers was observed in HWSS in all four BAV phenotypes. At the same time, collagen fibers in HWSS sites revealed striking helical and bundle-like structures, which are significantly different from those in LWSS, where the fibers appear more diffuse and randomly oriented.

Quantification of Fiber Contents and Orientations.To quantitatively analyze the images of the measured tissues,

which are usually at the size of $\sim 3 \text{ mm}^2$ (Figure S3) and taken at a fixed depth of 15 μ m, we applied fibers analysis using ImageJ and FiberFit software on each truncated tile (\sim 150 \times 150 μ m) and extracted the statistical results of the relative quantity of each type of fiber as well as their alignment anisotropy. As shown in Figure 7A, the relative abundance of collagen fibers was dramatically increased in BAV-NA patients compared to that in normal TAV patients, indicating extensive collagen proliferation. In contrast, BAV-AD patients exhibited a noticeable reduction in the collagen content (Figure 7B). Differences in elastin fibers, however, appeared to be less significant. Nevertheless, the relative quantities of either collagen or elastin between HWSS and LWSS in different BAV-AD phenotypes are not consistent and almost variable (Figure 7C and D), which may suggest that BAV-derived ascending aortic dilatation cannot be explained only by changes in the amount of collagen and elastin.

In the meantime, the anisotropy of the fiber alignments in different patients and two representative regions of 4 types of BAV patients were reflected in Figure 6B,E,F. Statistical analysis of images reveals that BAV-AD patients demonstrate the highest oriented collagen fibers architecture while BAV-NA patients also have a similar rise of anisotropy score in collagen fibers but not as statistically significant. Similarly, this feature also appeared on collagen fibers in the HWSS regions. The results of collagen fiber anisotropy revealed a convincing difference between HWSS and LWSS regions in each type of BAV patients. On the other hand, the situation of elastin fibers is more complicated. There is an overall increase of anisotropy in BAV-NA and BAV-AD patients, though they did not show a statistically significant difference compared to fibers in normal TAV patients. However, elastin fibers in HWSS regions demonstrate significantly higher alignment anisotropy than those in LWSS regions in most types of BAV.

The ideal surgical indication criterion for BAV aortopathy is to both minimize the risk of disastrous events and maximize the benefits of pre-emptive treatment and, in doing so, optimize clinical outcomes. Current international clinical guidelines^{5,6} recommend aortic root diameter as the threshold approach for the timing of intervention, which in certain extent, could reflect the hemodynamic abnormality as well as pathological progression^{38,39} but maybe too simplistic for risk-stratification and elective surgical decision-making.⁴⁰

Traditionally, people have considered aortic dissection to be the result of severe dilatation that imposes mechanical rupture. However, it is a disease incorporating various pathological changes in the medial layer of aorta, typically considered as fragmentation loss of elastic fibers, decreased smooth muscle cells, and increased proteoglycan deposition. In spite of the genesis inclination of aortic dilatation and dissection, a significantly high proportion of BAV patients does not progress at all, irrespective of BAV type. Therefore, this is of great theoretical and practical importance to introduce a reliable diagnostic tool, in parallel with the pathobiological phenomenon, to distinguish the "benign" from the "malignant" phenotypes of BAV disease.

In this study, we brought in a multimodal nonlinear optical microscopy, which specialized on intrinsic, label-free image and gained acceptance within many medical imaging fields, such as intraoperative diagnosis. Each one of the three inside modalities has its specific advantages. SRS microscopy can map the proper distribution of cell bodies as well as surrounding extracellular structures, ^{20,43} whereas SHG and

TPEF microscopy can detect the signals and autofluorescence from collagen and elastin. Although the imaging depth was generally limited to $\sim 200~\mu m$ for SRS, further improvement could be achieved by advanced tissue clearing methods to provide volumetric histology.

Consistent with previous reports, 45,46 we also found highly oriented collagen and elastin fibers in BAV-NA patients versus randomly distributed in normal TAV patients. Additionally, our results supported compensatory hyperplasia of collagen fibers in aortic media of BAV-NA patients, which is likely attributable to underlying intrinsic dysfunction. However, contrary to their results of BAV-AD patients as well as the tradition pathological understanding of this disease, our images and quantitative data revealed a remarkable decrease in the relative amount of collagen fibers, which form a structural network critical for limiting aortic distension.⁴⁷ The highly aligned helix-like and twisted morphology of collagen fibers could be hypothesized as a symbol of essential deformation (Figure 4), and it can be further verified by the outcome of different regional images of BAV-AD. This distinctive morphology of collagen fibers only exhibited in HWSS regions other than LWSS regions; meanwhile, collagen fibers orientation showed the same extent of alignment differences between regions in each BAV type. Moreover, combined with the trend of higher alignments of elastin fibers in HWSS, which could be interpreted as an accommodation of aorta dilatation, the overall discovery of collagen fibers provides a novel insight into the progression of BAV aortopathy. Our findings from obtained rapid histology of ascending aorta will be beneficial, from the translational perspective, for researchers to understand the pathophysiology of BAV aortopathy and assist surgeons with potential means of aortic risk evaluation.

However, some limitations are worth noting. Although our findings are promising, they should be validated in a more extensive and more diverse population, such as multicenter clinical trials. In addition, miniaturized devices with a fiber laser and hand-held probe are demanded for flexible applications in the clinic. Further work will focus on establishing a mathematical model to quantify the differences found in images and to create statistical results regarding the efficacy of NLO imaging data to predict the BAV patients' prognosis.

CONCLUSIONS

In summary, we have demonstrated the potential of multimodal NLO microscopy to image and detect architectural changes in ascending aorta of BAV patients, facilitating a rapid means of acquiring label-free tomographic histology on fresh tissues. Our data provide strong justification for the clinical implementation of histopathological diagnosis that stratifies the risk of aortic dissection and determines surgical treatment. We believe our method and finding provide the opportunity for improving the accuracy of intraoperative decision as well as a novel perspective for BAV and its underlying mechanism.

ASSOCIATED CONTENT

Supporting Information

The Supporting Information is available free of charge at https://pubs.acs.org/doi/10.1021/acs.analchem.5c04657.

Methods: 4D flow, histologic staining, and statistical analysis; quantitative analysis of the NLO images; SRS

and SHG images of large-scale tissues; and holistic image of a typical BAV-AD sample (PDF)

Video showing depth imaging in a typical HWSS region (MP4)

AUTHOR INFORMATION

Corresponding Authors

Jianpeng Ao — State Key Laboratory of Surface Physics and Department of Physics, Shanghai Key Laboratory of Metasurfaces for Light Manipulation, Endoscopy Center and Endoscopy Research Institute, Zhongshan Hospital, Fudan University, Shanghai 200433, China; Email: 20110190072@fudan.edu.cn

Wenshuo Wang — Department of Cardiac Surgery, Zhongshan Hospital, Fudan University, Shanghai 200030, China; Shanghai Engineering Research Center of Cardiac Valve, Shanghai 200433, China; Email: wang.wenshuo@zshospital.sh.cn

Minbiao Ji — State Key Laboratory of Surface Physics and Department of Physics, Shanghai Key Laboratory of Metasurfaces for Light Manipulation, Endoscopy Center and Endoscopy Research Institute, Zhongshan Hospital, Fudan University, Shanghai 200433, China; orcid.org/0000-0002-9066-4008; Email: minbiaoj@fudan.edu.cn

Authors

- Lili Zhang State Key Laboratory of Surface Physics and Department of Physics, Shanghai Key Laboratory of Metasurfaces for Light Manipulation, Endoscopy Center and Endoscopy Research Institute, Zhongshan Hospital, Fudan University, Shanghai 200433, China; Institute of Medical Chip, Ruijin Hospital, Shanghai Jiao Tong University School of Medicine, Shanghai 200025, China
- Yuntao Lu Department of Cardiac Surgery, Zhongshan Hospital, Fudan University, Shanghai 200030, China; Shanghai Engineering Research Center of Cardiac Valve, Shanghai 200433, China
- **Wencong Hong** Department of Oncology, The Hospital of Nanan City, Nanan 362300, China
- Shuo Cong Department of Cardiac Surgery, Zhongshan Hospital, Fudan University, Shanghai 200030, China; Shanghai Engineering Research Center of Cardiac Valve, Shanghai 200433, China
- Jiaying Li State Key Laboratory of Surface Physics and Department of Physics, Shanghai Key Laboratory of Metasurfaces for Light Manipulation, Endoscopy Center and Endoscopy Research Institute, Zhongshan Hospital, Fudan University, Shanghai 200433, China
- Huan Liu Department of Cardiac Surgery, Zhongshan Hospital, Fudan University, Shanghai 200030, China; Shanghai Engineering Research Center of Cardiac Valve, Shanghai 200433, China
- Chunsheng Wang Department of Cardiac Surgery, Zhongshan Hospital, Fudan University, Shanghai 200030, China; Shanghai Engineering Research Center of Cardiac Valve, Shanghai 200433, China
- Lai Wei Department of Cardiac Surgery, Zhongshan Hospital, Fudan University, Shanghai 200030, China; Shanghai Engineering Research Center of Cardiac Valve, Shanghai 200433, China

Complete contact information is available at: https://pubs.acs.org/10.1021/acs.analchem.5c04657

Author Contributions

*L.Z., Y.L., and W.H. contributed equally. M. Ji, W. Wang, J. Ao and L. Wei conceived the work. Li. Zhang and J. Li performed SRS measurements and data analysis. H. Liu and S. Cong helped with tissue preparation and medical data. L. Zhang, W. Wang, and M. J. wrote the manuscript, and all authors reviewed and approved it.

Notes

The authors declare no competing financial interest.

ACKNOWLEDGMENTS

We thank the financial support from the National Key R&D Program of China (2021YFF0502900); National Natural Science Foundation of China (62425501); Municipal Natural Science Foundation of Shanghai (23dz2260100); Shanghai Municipal Science and Technology Commission (17YF1402100); Research Project of Zhongshan Hospital (2019ZSYQ05); and Shanghai Key Laboratory of Female Reproductive Endocrine Related Diseases.

REFERENCES

- (1) Longobardo, L.; Jain, R.; Carerj, S.; Zito, C.; Khandheria, B. K. Am. J. Med. 2016, 129 (8), 796–805.
- (2) Michelena, H. I.; Corte, A. D.; Prakash, S. K.; Milewicz, D. M.; Evangelista, A.; Enriquez-Sarano, M. *Int. J. Cardiol.* **2015**, 201, 400–407
- (3) Michelena, H. I.; Prakash, S. K.; Della Corte, A.; Bissell, M. M.; Anavekar, N.; Mathieu, P.; Bossé, Y.; Limongelli, G.; Bossone, E.; Benson, D. W.; et al. *Circulation* **2014**, *129* (25), 2691–2704.
- (4) Hiratzka, L. F.; Creager, M. A.; Isselbacher, E. M.; Svensson, L. G.; Nishimura, R. A.; Bonow, R. O.; Guyton, R. A.; Sundt, T. M. J. Am. Coll. Cardiol. **2016**, 67 (6), 724–731.
- (5) Baumgartner, H.; Falk, V.; Bax, J. J.; De Bonis, M.; Hamm, C.; Holm, P. J.; Iung, B.; Lancellotti, P.; Lansac, E.; Rodriguez Munoz, D. Eur. Heart J. 2017, 38 (36), 2739–2791.
- (6) Borger, M. A.; Fedak, P. W.; Stephens, E. H.; Gleason, T. G.; Girdauskas, E.; Ikonomidis, J. S.; Khoynezhad, A.; Siu, S. C.; Verma, S.; Hope, M. D.; et al. *J. Thorac. Cardiovasc. Surg.* **2018**, *156* (2), 473–480.
- (7) Freudiger, C. W.; Min, W.; Saar, B. G.; Lu, S.; Holtom, G. R.; He, C.; Tsai, J. C.; Kang, J. X.; Xie, X. S. Science **2008**, 322 (5909), 1857–1861.
- (8) Denk, W.; Strickler, J. H.; Webb, W. W. Science 1990, 248 (4951), 73-76.
- (9) Cohen, B. E. Nature 2010, 467 (7314), 407-408.
- (10) Ma, L.; Luo, K.; Liu, Z.; Ji, M. Anal. Chem. 2024, 96 (20), 7907–7925.
- (11) Jiang, L.; Wang, X.; Wu, Z.; Du, H.; Wang, S.; Li, L.; Fang, N.; Lin, P.; Chen, J.; Kang, D.; et al. *Laser Phys. Lett.* **2017**, *14* (10), 105401.
- (12) Yang, Y. F.; Chen, L. C.; Ji, M. B. J. Innovative Opt. Health Sci. 2017, 10 (5), 1730010.
- (13) Zhang, L.; Zou, X.; Zhang, B.; Cui, L.; Zhang, J.; Mao, Y.; Chen, L.; Ji, M. *Theranostics* **2018**, 8 (15), 4129–4140.
- (14) Eibl, M.; Karpf, S.; Hakert, H.; Weng, D.; Huber, R.. In Two-photon-excited fluorescence (TPEF) and fluorescence lifetime imaging (FLIM) with sub-nanosecond pulses and a high analog bandwidth signal detection; SPIE, 2017.
- (15) Wang, H.-W.; Le, T. T.; Cheng, J.-X. Opt. Commun. 2008, 281 (7), 1813–1822.
- (16) Chen, X.; Nadiarynkh, O.; Plotnikov, S.; Campagnola, P. J. *Nat. Protoc.* **2012**, *7* (4), 654–669.
- (17) Bianchini, P.; Diaspro, A. J. Biophotonics 2008, 1 (6), 443–450.
- (18) Freund, I.; Deutsch, M. Opt. Lett. 1986, 11 (2), 94–96.
- (19) Saar, B. G.; Freudiger, C. W.; Reichman, J.; Stanley, C. M.; Holtom, G. R.; Xie, X. S. Science **2010**, 330 (6009), 1368–1370.

- (20) Ji, M.; Orringer, D. A.; Freudiger, C. W.; Ramkissoon, S.; Liu, X.; Lau, D.; Golby, A. J.; Norton, I.; Hayashi, M.; Agar, N. Y. R.; et al. Sci. Transl. Med. 2013, 5 (201), 201ra119.
- (21) Liu, Z.; Su, W.; Ao, J.; Wang, M.; Jiang, Q.; He, J.; Gao, H.; Lei, S.; Nie, J.; Yan, X.; et al. Nat. Commun. 2022, 13 (1), 4050.
- (22) Zhang, L.; Zou, X.; Huang, J.; Fan, J.; Sun, X.; Zhang, B.; Zheng, B.; Guo, C.; Fu, D.; Yao, L.; et al. *Anal. Chem.* **2021**, 93 (46), 15550–15558.
- (23) Ao, J.; Shao, X.; Liu, Z.; Liu, Q.; Xia, J.; Shi, Y.; Qi, L.; Pan, J.; Ji, M. Cancer Res. **2023**, 83 (4), 641–651.
- (24) Zhang, D.; Chen, W.; Chen, H.; Yu, H.-Q.; Kassab, G.; Cheng, J.-X. J. Biophotonics **2018**, 11 (2), No. e201700005.
- (25) Zhang, L.; Wu, Y.; Zheng, B.; Su, L.; Chen, Y.; Ma, S.; Hu, Q.; Zou, X.; Yao, L.; Yang, Y.; et al. *Theranostics* **2019**, *9* (9), 2541–2554.
- (26) Ji, M.; Lewis, S.; Camelo-Piragua, S.; Ramkissoon, S. H.; Snuderl, M.; Venneti, S.; Fisher-Hubbard, A.; Garrard, M.; Fu, D.; Wang, A. C.; et al. *Sci. Transl. Med.* **2015**, 7 (309), 309ra163.
- (27) Wu, Y.; Fu, F.; Lian, Y.; Nie, Y.; Zhuo, s.; Wang, C.; Chen, J. J. Phys. D: Appl. Phys. **2015**, 48 (40), 405401.
- (28) Ji, M.; Arbel, M.; Zhang, L.; Freudiger, C. W.; Hou, S. S.; Lin, D.; Yang, X.; Bacskai, B. J.; Xie, X. S. Sci. Adv. 2018, 4 (11), No. eaat7715.
- (29) Zhang, B.; Sun, M.; Yang, Y.; Chen, L.; Zou, X.; Yang, T.; Hua, Y.; Ji, M. Biomed. Opt. Express 2018, 9 (6), 2604-2613.
- (30) He, R.; Xu, Y.; Zhang, L.; Ma, S.; Wang, X.; Ye, D.; Ji, M. Optica 2017, 4 (1), 44–47.
- (31) He, R.; Liu, Z.; Xu, Y.; Huang, W.; Ma, H.; Ji, M. Opt. Lett. **2017**, 42 (4), 659–662.
- (32) Zhang, B.; Xu, H.; Chen, J.; Zhu, X.; Xue, Y.; Yang, Y.; Ao, J.; Hua, Y.; Ji, M. *Theranostics* **2021**, *11* (7), 3074–3088.
- (33) Ayyalasomayajula, V.; Pierrat, B.; Badel, P. Biomech. Model. Mechanobiol. 2019, 18 (5), 1507-1528.
- (34) Girdauskas, E.; Borger, M. A.; Secknus, M.-A.; Girdauskas, G.; Kuntze, T. Eur. J. Cardio. Thorac. Surg. 2011, 39 (6), 809–814.
- (35) Guzzardi, D. G.; Barker, A. J.; van Ooij, P.; Malaisrie, S. C.; Puthumana, J. J.; Belke, D. D.; Mewhort, H. E.; Svystonyuk, D. A.; Kang, S.; Verma, S.; et al. *J. Am. Coll. Cardiol.* **2015**, *66* (8), 892–900.
- (36) Mahadevia, R.; Barker, A. J.; Schnell, S.; Entezari, P.; Kansal, P.; Fedak, P. W.; Malaisrie, S. C.; McCarthy, P.; Collins, J.; Carr, J.; et al. *Circulation* **2014**, *129* (6), *673*–682.
- (37) Sievers, H.-H.; Schmidtke, C. J. Thorac. Cardiovasc. Surg. **2007**, 133 (5), 1226–1233.
- (38) Girdauskas, E.; Rouman, M.; Disha, K.; Fey, B.; Dubslaff, G.; Theis, B.; Petersen, I.; Gutberlet, M.; Borger, M. A.; Kuntze, T. *J. Am. Coll. Cardiol.* **2016**, *67* (15), 1786–1796.
- (39) Bürk, J.; Blanke, P.; Stankovic, Z.; Barker, A.; Russe, M.; Geiger, J.; Frydrychowicz, A.; Langer, M.; Markl, M. J. Cardiovasc. Magn. Reson. 2012, 14 (1), 84.
- (40) Gagné-Loranger, M.; Dumont, E. .; Voisine, P.; Mohammadi, S.; Dagenais, F. Eur. J. Cardio. Thorac. Surg. 2016, 50 (3), 562–566.
- (41) Michelena, H. I.; Prakash, S. K.; Della Corte, A.; Bissell, M. M.; Anavekar, N.; Mathieu, P.; Bossé, Y.; Limongelli, G.; Bossone, E.; Benson, D. W.; et al. *Circulation* **2014**, *129* (25), 2691–2704.
- (42) Detaint, D.; Michelena, H. I.; Nkomo, V. T.; Vahanian, A.; Jondeau, G.; Sarano, M. E. *Heart* **2014**, *100* (2), 126–134.
- (43) Yang, Y.; Yang, Y.; Liu, Z.; Guo, L.; Li, S.; Sun, X.; Shao, Z.; Ji, M. Anal. Chem. **2021**, 93 (15), 6223–6231.
- (44) Wei, M.; Shi, L.; Shen, Y.; Zhao, Z.; Guzman, A.; Kaufman, L. J.; Wei, L.; Min, W. Proc. Natl. Acad. Sci. U.S.A. 2019, 116 (14), 6608–6617
- (45) Phillippi, J. A.; Green, B. R.; Eskay, M. A.; Kotlarczyk, M. P.; Hill, M. R.; Robertson, A. M.; Watkins, S. C.; Vorp, D. A.; Gleason, T. G. J. Thorac. Cardiovasc. Surg. 2014, 147 (3), 1056–1064.
- (46) Tsamis, A.; Phillippi, J. A.; Koch, R. G.; Chan, P. G.; Krawiec, J. T.; D'Amore, A.; Watkins, S. C.; Wagner, W. R.; Vorp, D. A.; Gleason, T. G. J. Thorac. Cardiovasc. Surg. 2016, 151 (6), 1718–1728.
- (47) Ross, M. H.; Pawlina, W. Histology: A Text and Atlas: With Correlated Cell and Molecular Biology; Lippincott Williams & Wilkins, a Wolters Kluwer business, 2011.



Subscribe today